

High-redshift quasars at $z \geq 3$ – I. Radio spectra

Yu. Sotnikova,^{1*} A. Mikhailov,¹ T. Mufakharov,^{1,2,3} M. Mingaliev,^{1,2} N. Bursov,¹ T. Semenova,¹
V. Stolyarov,^{1,2,4} R. Udovitskiy,¹ A. Kudryashova¹ and A. Erkenov¹

¹*Special Astrophysical Observatory of RAS, Nizhny Arkhyz, 369167, Russia*

²*Kazan Federal University, 18 Kremlyovskaya St, Kazan 420008, Russia*

³*Shanghai Astronomical Observatory, Chinese Academy of Sciences, Shanghai 200030, China*

⁴*Astrophysics Group, Cavendish Laboratory, University of Cambridge, J J Thomson Avenue, Cambridge CB3 0HE, UK*

Accepted 2021 July 16. Received 2021 July 09; in original form 2021 April 22

ABSTRACT

We present the radio properties of optically selected quasars with $z \geq 3$. The complete sample consists of 102 quasars with a flux density level $S_{1.4} \geq 100$ mJy in a declination range $-35^\circ \leq \text{Dec} \leq +49^\circ$. The observations were obtained in 2017–2020 using the radio telescope RATAN-600. We measured flux densities at six frequencies 1.2, 2.3, 4.7, 8.2, 11.2, and 22 GHz quasi-simultaneously with uncertainties of 9–31 per cent. The detection rate is 100, 89, and 46 per cent at 4.7, 11.2, and 22 GHz, respectively. We have analysed the averaged radio spectra of the quasars based on the RATAN and literature data. We classify 46 per cent of radio spectra as peaked-spectrum, 24 per cent as flat, and none as ultra-steep spectra ($\alpha \leq -1.1$). The multifrequency data reveal that a peaked spectral shape (PS) is a common feature for bright high-redshift quasars. This indicates the dominance of bright compact core emission and the insignificant contribution of extended optically thin kpc-scale components in observed radio spectra. Using these new radio data, the radio loudness $\log R$ was estimated for 71 objects with a median value of 3.5, showing that the majority of the quasars are highly radio-loud with $\log R > 2.5$. We have not found any significant correlation between z and α . Several new megahertz-peaked spectrum (MPS) and gigahertz-peaked spectrum (GPS) candidates are suggested. Further studies of their variability and additional low-frequency observations are needed to classify them precisely.

Key words: galaxies: active – galaxies: high-redshift – quasars: general – radio continuum: galaxies

1 INTRODUCTION

High-redshift ($z \geq 3$) quasars are important to study because they provide information about the growth of supermassive black holes and the evolution of active galactic nuclei (AGNs) in the early Universe. Most of high-redshift and radio-loud objects are expected to be blazars, a subclass of AGNs with a relativistic jet pointing toward the observer (Urry & Padovani 1995). Relativistically beamed sources dominate the high-redshift radio source population due to the Doppler boosting effect. The number of radio-loud ($R_{1.4} \geq 100$) quasars decreases with increasing redshift. For example, at $z > 6$ only several radio-loud quasars are found, and radio emission is not detected at $z > 7$ in optically detected quasars (Wang et al. 2007; Momjian et al. 2014).

An observed radio spectrum of a blazar is a combination of a flat spectrum by a compact core and a steep spectrum by a kiloparsec jet. The relationship between the core and the jet power determines the shape of the observed radio spectrum based on their contribution. Hence, the majority of radio sources at high redshifts should have a flat spectrum. How-

ever, we observe the well-known steep-spectrum (Momjian et al. 2008; Frey et al. 2008, 2010) and the gigahertz-peaked spectrum (GPS) population high-redshift radio-loud quasars (O’Dea 1990; Frey et al. 2010).

Currently, only a few high-redshift blazars are found at $z \geq 5$, for example SDSS J114657.79+403708.6 (Frey et al. 2010; Ghisellini et al. 2014), SDSS J102623.61+254259.5 (Sbarrato et al. 2012; Frey et al. 2015), SDSS J164854+460328 (Caccianiga et al. 2019), Q0906+6930 (Romani et al. 2004), and PSO J047.4478+27.2992 (Belladitta et al. 2020). Their radio loudness is much less than that of quasars at redshifts $3 \leq z \leq 5$.

The most distant known blazar at $z = 6.1$, PSO J047.4478+27.2992, was discovered by Belladitta et al. (2020) in 2020 and is considered a compact steep-spectrum or a megahertz-peaked spectrum (CSS/MPS) candidate based on the RATAN-600 and Very Large Array (VLA) measurements (Spingola et al. 2020; Mufakharov et al. 2021). It is a radio-loud blazar with a $\log R \sim 2.5$, which is higher by several orders of magnitude than for quasars at $z = 3$ –5.

Several studies have compiled and studied statistically high-redshift blazars based on the optical (Sloan Digital Sky Survey (SDSS), e.g. Sbarrato et al. 2013) or radio (Cosmic Lens All Sky Survey (CLASS)) observations (e.g. Cac-

* E-mail: lacertae999@gmail.com

cianiga et al. 2019). A systematic study of 30 high-redshift ($z > 4.5$) quasars was presented by Coppejans et al. (2016b, 2017), where multifrequency radio spectra were used to classify the spectral type of the sources and no preferable spectral type for high-redshift objects was found. Blumenthal & Miley (1979), Tielens et al. (1979), Laing & Peacock (1980), and De Breuck et al. (2000) demonstrated that sources with higher redshifts had steeper radio spectra. In some studies an ultra-steep spectrum is used either as an indicator of high redshift (e.g. Jarvis et al. 2001; Singh et al. 2014) or as a reasonable tracer of intermediate-redshift ($z \geq 1$) galaxies (Smolčić et al. 2014). There are only four radio-loud quasars known at $z > 6$ to date, PSO J172.3556+18.7734 at $z = 6.82$ is the most distant among them (Bañados et al. 2021). It has a steep radio spectrum ($\alpha_{1.5-3} = -1.31$) and radio loudness about $R_{4400} \sim 70$.

Unfortunately, for most quasars at $z > 3$ observed data are available at very few radio frequencies. In this study, new RATAN-600 observed data for 102 high-redshift quasars are presented. In 2017–2020 we obtained radio spectra measured quasi-simultaneously at 1.2, 2.3, 4.7, 8.2, 11.2, and 22 GHz and compiled a catalogue of six-frequency flux densities. Combining our new observations with those from the literature, we investigated the radio spectra of quasars at $z \geq 3$. We estimated the radio luminosity and radio loudness for these objects and made an analysis for different redshift ranges. Spectral classification was performed and new GPS/MPS candidates were found.

2 THE SAMPLE

The complete sample consists of 102 quasars at $z \geq 3$ with a flux density level $S_{1.4} \geq 100$ mJy in the declination range $-35^\circ \leq \text{Dec} \leq 49^\circ$ (Fig. 1).

The spectroscopic redshifts were taken from the National Aeronautics and Space Administration (NASA)/Infrared Processing and Analysis Center (IPAC) Extragalactic Database (NED),¹ and the redshift median value was found to be 3.26. There are 10 quasars at $z \geq 4$ in the sample and only one, B2 1023+25, at $z > 5$ ($z = 5.28$; Sbarrato et al. (2012)). The number of objects decreases exponentially with increasing redshift (Fig. 2). There are 22 bright radio quasars with flux densities 0.5–2.4 Jy in the sample, and the median value of the flux density at 1.4 GHz is 0.22 Jy (Fig. 3).

Table 1 presents the list of the sources with their characteristics, where Column 1 is the source name, Column 2 is the redshift z , Column 3 is the average flux density at 4.7 GHz (RATAN-600 measurements), Column 4 is the radio luminosity at 4.7 GHz, Column 5 is the radio loudness $\log R$, Columns 6 and 7 are the spectral indices, Column 8 is the radio spectrum type, and Column 9 is the blazar type.

The list includes 48 quasars that are classified as blazars according to the 5th Edition of the Roma-BZCAT catalogue (Massaro et al. 2015). Almost all blazars (46) are flat-spectrum radio quasars (FSRQs), and two of them are blazars of an uncertain type.

For high-energy bands, we found that only seven sources have their matches in the *Fermi*-LAT 4th catalog (Ballet

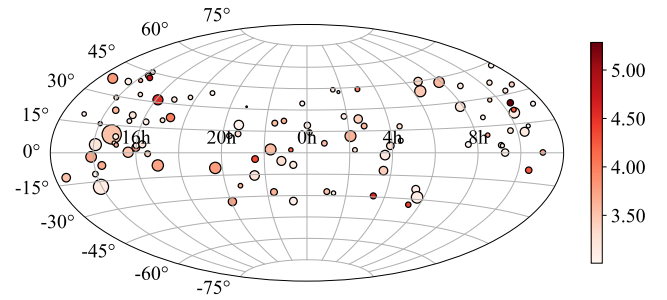


Figure 1. Hammer-Aitoff projection in galactic coordinates of the sky distribution of the quasars. The size of the circles corresponds to the flux density level at 1.4 GHz, and the color indicates the redshift value.

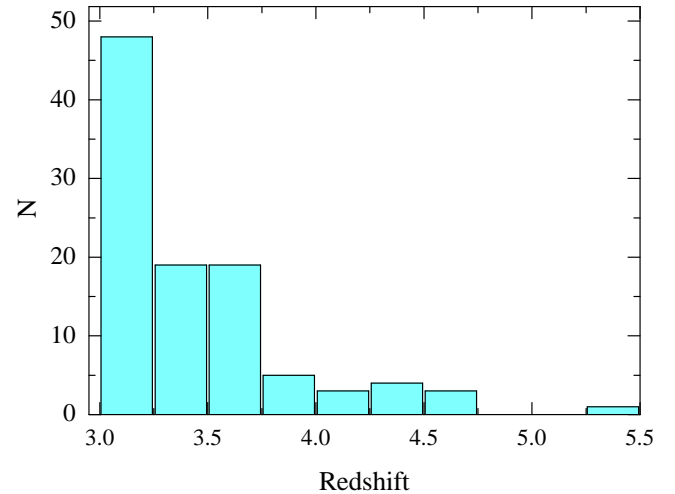


Figure 2. Redshift distribution for the sample.

et al. 2020), and 30 sources have X-ray photon fluxes available according to the NED database.

3 OBSERVATIONS AND DATA REDUCTION

We carried out the observations in transit mode with the RATAN-600 radio telescope (Parijskij 1993; Sotnikova 2020) at six frequencies between 1.2 and 22 GHz simultaneously. For a single transit observation, one can obtain an instantaneous spectrum of a source. RATAN-600 continuum radiometer parameters are presented in Sotnikova et al. (2019a).

The sample was observed in 2017–2020. We observed the sources 3–15 times for each observing epoch to improve the signal-to-noise (S/N) ratio. The median number of the observing epochs is $N_{\text{obs}} = 9$ for the sample.

The observations were processed using the Flexible Astronomical Data Processing System (FADPS) standard data reduction software developed by Verkhodanov (1997) for the broadband RATAN-600 continuum radiometers and the automated data reduction system (Tsybulev 2011; Tsybulev et al. 2018; Udovitskiy et al. 2016). We used the following eight flux density secondary calibrators: 3C48, 3C138, 3C147, 3C161, 3C286, 3C295, 3C309.1, and NGC 7027. The flux-density scale is based on measurements by Baars et al.

¹ <https://ned.ipac.caltech.edu>

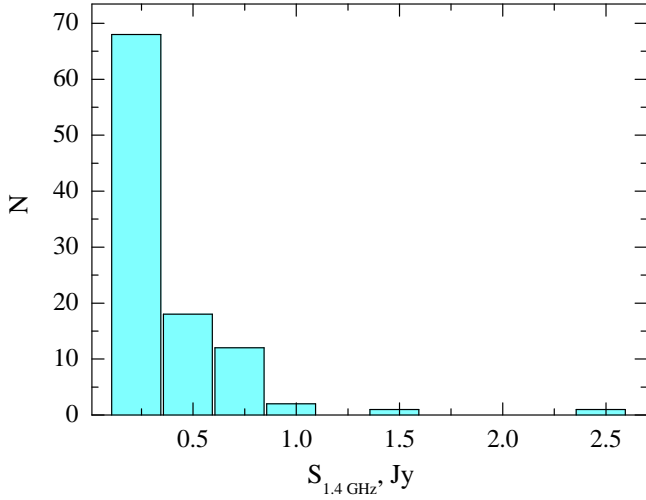


Figure 3. Flux density distribution for the sample at 1.4 GHz.

(1977) and Perley & Butler (2013, 2017); these are in good agreement, and their differences are within the measurement errors. Additionally we used traditional RATAN-600 flux density calibrators: J0240-23, J1154-35, and J0521+16 (Sotnikova et al. 2019b). The measurements of the calibrators were corrected for angular size and linear polarisation, according to the data from Ott et al. (1994) and Tabara & Inoue (1980).

The measurement uncertainties and the calibration procedure are described in Mingaliev et al. (2001) and Mufakharov et al. (2021).

4 RESULTS

4.1 Flux densities

The total number of observations is more than 1400, and the detection rates are 46 per cent and 100 per cent at 22 and 4.7 GHz, respectively (Table 1). The number of sources with RATAN data available at five to six frequencies is 75. The median value of the S/N ratio varies from 9 to 17 at 4.7–22 GHz. At 1.2 and 2.3 GHz, the median S/N values are 25 and 31 due to strong radio frequency interference (RFI). The strong RFI contamination at 11.2 GHz is also the reason for the non-detection of objects in the declination range $-10^\circ \leq \text{Dec.} \leq 0^\circ$.

The flux density standard errors are 5–20 per cent for 11.2, 8.2, and 4.7 GHz, and 10–35 per cent for 2.3, 1.2, and 22 GHz. Table 1 presents the detection rate statistics, median flux densities, and their uncertainties for different frequencies. Fig. 4 presents the average flux density distribution at the six frequencies.

Table 2 presents the flux densities, where Columns 1 and 2 are the source name and the averaged observing epoch (JD), Columns 3–14 are the flux densities and their uncertainties (Jy). The data is distributed in the Vizier Information System.² The RATAN-600 flux densities and the instantaneous spectra for some quasars are published in the BL Lac

Table 1. Observational statistics: the mean value of the RATAN flux densities \bar{S} and their uncertainties $\bar{\sigma}_S$, number of observations N_{obs} , and detection rates. The standard deviations are given in parentheses.

Frequency (GHz)	\bar{S} (Jy)	$\bar{\sigma}_S$ (%)	N_{obs}	Detections (%)
22	0.56 (0.59)	18	1418	46
11.2	0.41 (0.55)	11	1418	89
8.2	0.32 (0.51)	11	801	99
4.7	0.44 (0.52)	9	1418	100
2.3	0.38 (0.37)	31	801	82
1.2	0.77 (0.50)	25	801	12

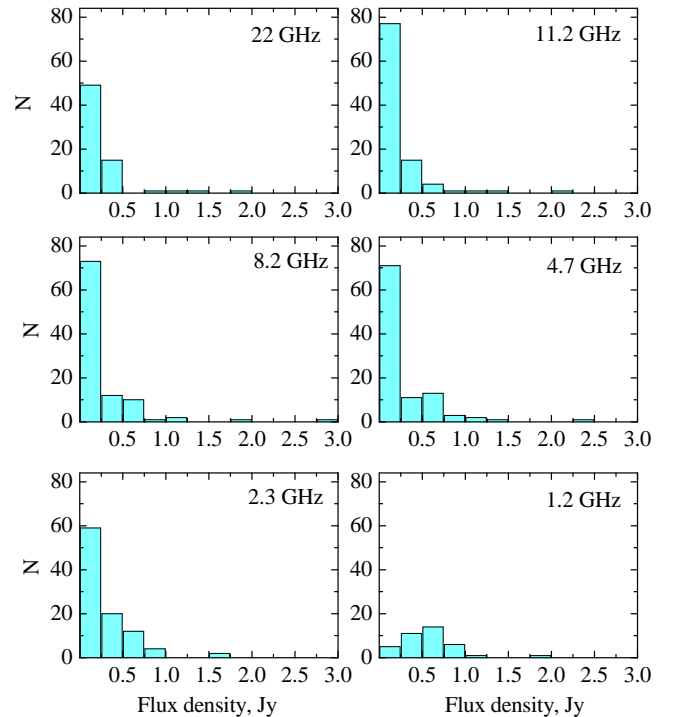


Figure 4. Averaged flux density distributions for the sample at RATAN frequencies.

database³ maintained by the Special Astrophysical Observatory. The database is constantly updated with new data and is freely available (Mingaliev et al. 2014).

4.2 Radio spectra and classification

Figs. 1–5 show the broad-band radio spectra of the quasars. We compiled the spectra using both RATAN (red circles) and CATS (black circles) data (Verkhodanov et al. 2005, 1997). The RATAN-600 measurements cover the time period 2017–2020, except for several objects which were observed from 2014. The CATS data cover a time period of several dozens years, and the main data are represented by the National Radio Astronomy Observatory (NRAO) VLA Sky Survey (NVSS: Condon et al. (1998)), Faint Images of the Radio

² <https://vizier.u-strasbg.fr/viz-bin/VizieR>

³ www.sao.ru/blcat/

Table 2. RATAN-600 flux densities for 102 quasars, measured simultaneously at six frequencies (1.2–22 GHz). A sample is shown here; the full version is available as online supporting material.

NVSS name	JD	S_{22}	$S_{11.2}$	$S_{8.2}$	$S_{4.7}$	$S_{2.3}$	$S_{1.2}$
000108+191434	2457793	–	0.168 ± 0.016	0.166 ± 0.017	0.167 ± 0.015	0.151 ± 0.055	–
000108+191434	2457838	0.104 ± 0.023	0.134 ± 0.014	0.156 ± 0.016	0.190 ± 0.017	0.207 ± 0.055	–
000108+191434	2457853	0.147 ± 0.029	0.129 ± 0.013	0.155 ± 0.016	0.150 ± 0.013	0.136 ± 0.055	–
000108+191434	2458027	0.146 ± 0.029	0.135 ± 0.014	0.150 ± 0.015	0.164 ± 0.014	0.207 ± 0.055	0.339 ± 0.096
000108+191434	2458104	0.111 ± 0.024	0.126 ± 0.013	0.141 ± 0.015	0.170 ± 0.015	0.167 ± 0.055	–
000108+191434	2458192	–	0.108 ± 0.012	0.133 ± 0.014	0.157 ± 0.014	0.144 ± 0.055	–
000108+191434	2458236	–	0.129 ± 0.013	0.151 ± 0.016	0.153 ± 0.013	0.167 ± 0.055	–
000108+191434	2458309	0.112 ± 0.024	0.117 ± 0.012	0.152 ± 0.016	0.168 ± 0.015	0.194 ± 0.055	–
000108+191434	2458530	–	0.094 ± 0.010	0.107 ± 0.012	0.134 ± 0.012	0.153 ± 0.055	–
000108+191434	2458717	0.103 ± 0.022	0.119 ± 0.012	0.118 ± 0.013	0.139 ± 0.012	0.125 ± 0.056	0.181 ± 0.067
000108+191434	2458771	–	0.088 ± 0.010	0.106 ± 0.012	0.120 ± 0.011	0.122 ± 0.056	–

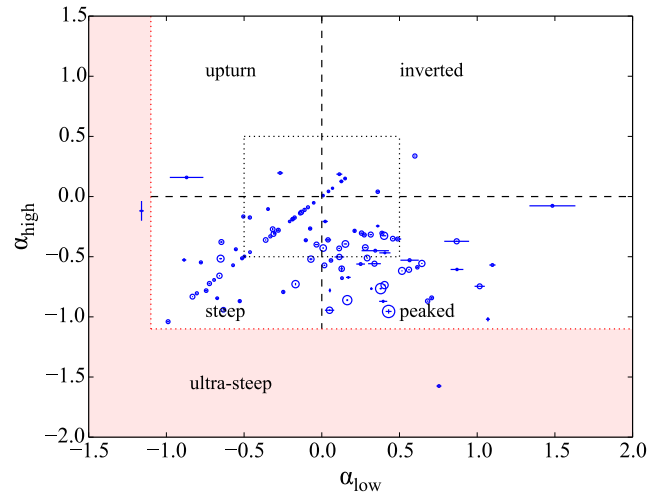
Sky at Twenty cm (FIRST: Becker et al. (1994)), Westerbork Northern Sky Survey (WENSS: Rengelink et al. (1997)), Green Bank 6-cm survey (GB6: Gregory et al. (1996)), Australia Telescope 20 GHz Survey (ATCA20: Murphy et al. (2010)), and VLA measurements. Low-frequency data are well presented by the GaLactic and Extragalactic All-sky Murchison Widefield Array (GLEAM) survey at 72–231 MHz (2013–2014; Hurley-Walker et al. (2017)) and the Giant Metrewave Radio Telescope Sky Survey (TGSS) at 150 MHz (2015, Intema et al. (2017)); the data were obtained almost simultaneously with the RATAN-600 observations.

We analysed the averaged radio spectra of quasars compiled from the RATAN and CATS data. The spectral parameters were estimated by fitting with polynomials, which were calculated by weight averaging of measurements in the FADPS software package (Verkhodanov et al. 1997). The resulting approximations are shown by the green dotted lines in Figs. 1–5. We defined the spectral index from the power-law $S_\nu \propto \nu^\alpha$ (S_ν is a flux density at the frequency ν , and α is a spectral index).

Table 3 presents the criteria based on which the spectral classification was made. We determined the spectral indices α_{low} and α_{high} for peaked and upturn spectra for the frequencies where the spectral slope changes its sign from positive to negative or vice versa. For the rest of the spectra, the low-frequency spectral index was calculated between the TGSS, GLEAM, WENSS, and other decimeter-wavelength measurements. The high-frequency spectral index was estimated between centimeter catalog data points. We considered a spectrum to be flat if the spectral index $-0.5 \leq \alpha \leq 0$, and inverted if $\alpha > 0$. The spectrum is assumed to be complex for indeterminate shapes with two or more maxima or minima. The spectrum is called steep or ultra-steep for $-1.1 < \alpha < -0.5$ and $\alpha \leq -1.1$, respectively.

Fig. 5 presents the spectral-type distribution in the convenient form of a two-color diagram in which α_{low} is plotted against α_{high} . The point size is proportional to the radio luminosity at 4.7 GHz. The ‘blazar box’ corresponds to the spectral index range from -0.5 to 0.5 . The median values of α_{low} and α_{high} are -0.01 (0.52) and -0.44 (0.33), respectively (Fig. 6). Thus, the majority of the radio spectra steepens at higher frequencies.

We found 47 (46 per cent) of quasars had peaked radio spectra (PS) with a turnover in their average spectrum (Table 2). There are 17 sources with classical (de Vries et al.

**Figure 5.** Two-color diagram. The dotted square indicates the ‘blazar box’, the dashed lines mark the zero spectral indices, and the ultra-steep spectrum sources area is presented with a pink color. The point size is proportional to the radio luminosity at 4.7 GHz.

1997) GPS spectral features and 13 quasars with a peak at MHz frequencies (MPS). We present 24 new GPS and MPS candidates in Table 2.

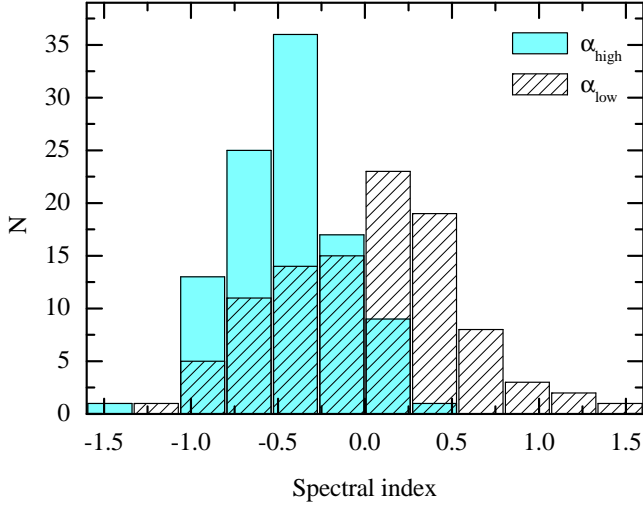
A large part of the sample (24 per cent) has flat spectra and 15 per cent has steep ones. A small number of the sources have complex, upturn, and inverted spectra.

We have not found ultra-steep radio spectra. The spectrum of PKS 2313-330 has an ultra-steep part with $\alpha_{4.7-11.2} = -1.58 \pm 0.09$ and is classified as PS. The spectral index was determined based on the multi-epoch RATAN observations in 2015–2020 at four frequencies simultaneously. For the second quasar, 87GB 012817.1+434250, we found an ultra-steep spectral part at low frequencies with $\alpha_{1.4-4.7} = -1.16 \pm 0.02$. This object is classified as having a complex spectrum. Its ultra-steep spectral part was obtained from two non-simultaneous measurements (NVSS and RATAN) on a time-scale of 20 years.

For nine quasars, the radio spectra are well described by a sum of two spectral components at low (LFC) and high (HFC) frequencies (Kovalev et al. 2002, 2020), which are denoted by ‘*’ in Table 1. LFC indicates an optically thin

Table 3. Spectral types in the sample.

Type	Criteria	N	%
Peaked	$\alpha_{\text{low}} > 0, \alpha_{\text{high}} < 0$	47	46
Flat	$-0.5 \leq \alpha \leq 0$	25	24
Inverted	$\alpha > 0$	8	8
Upturn	$\alpha_{\text{low}} < 0, \alpha_{\text{high}} > 0$	2	2
Steep	$-1.1 < \alpha < -0.5$	15	15
Ultra-steep	$\alpha \leq -1.1$	0	0
Complex	Two or more maxima/minima	5	5


Figure 6. Distribution of the low-frequency (shaded) and high-frequency (colored) spectral indices for the averaged radio spectra.

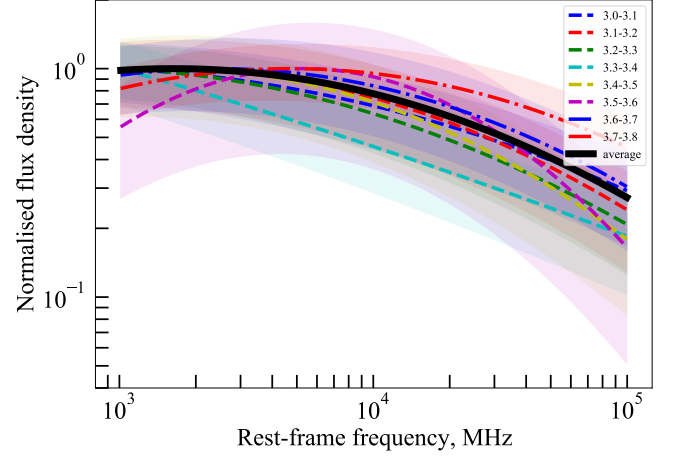
synchrotron emission of extended kpc-scale structures with a peak frequency much less than 1 GHz due to its characteristic size (Slish 1963). HFC dominates at frequencies of several GHz and more and is associated with the pc-scale jet.

4.3 The average spectrum

To study the distant radio sources population, we used continuum radio spectra averaged over the objects located within close redshift intervals $\Delta z = 0.1$. The spectrum of each object was preliminarily recalculated into the rest frame using the $(1+z)$ correction. The spectra of individual objects were then approximated by a polynomial of the first or second degree. Finally, the average spectrum of all objects in each bin was calculated using the formula (Verkhodanov et al. 2018)

$$\log S(\nu_j) = \frac{1}{N} \sum_{i=1}^N \log f_i(\nu_j), \quad (1)$$

where ν_j is the set of frequencies in the approximating data set for the i th source, $f_i(\nu_j)$ is the flux density calculated for the i th source approximation at a frequency ν_j , and N is the number of sources. The averaging procedure was carried out using the *spcalc* utility of the FADPS data processing system. As a result, we have calculated eight average spectra in the range $z = 3.0\text{--}3.8$. The mean error of the averaged spectrum in each redshift bin is determined by the quadratic sum of spectrum approximation uncertainties. The uncertainty of


Figure 7. Average spectra of the sources normalised by the peak flux density. The coloured lines relate to the redshift bins $z = 3.0\text{--}3.8$ and corresponding strips represent 3σ uncertainties. The black line is the average spectrum of all sources at $z = 3.0\text{--}3.8$.

the spectrum approximation of an individual object was calculated using errors of polynomial fitting coefficients by a standard method. At higher redshift intervals, there are only a few objects, and the averaging procedure was not applied.

Fig. 7 presents the normalised average radio spectra for the redshift bins $\Delta z = 0.1$. The cumulative radio spectrum is shown by the black line. A 99 per cent confidence intervals (3σ) are shown as strips with different colors.

The eight average spectra in the redshifts range 3.0–3.8 show a similar shape within their uncertainties. The values of low and high spectral indices for the cumulative radio spectrum are $\alpha_{\text{low}} = 0.20 \pm 0.03$ and $\alpha_{\text{high}} = -0.40 \pm 0.02$, respectively. The peak frequency for the average spectrum is about 1.6 GHz in the rest frame.

4.4 $z\text{--}\alpha$ correlation

We have not found any significant correlation between redshifts and spectral indices at low and high frequencies (Fig. 8). The Pearson correlation coefficient is $r = 0.07$ for $\alpha_{\text{low}} - z$ and $r = 0.01$ for $\alpha_{\text{high}} - z$, with 46 and 95 per cent of probability that these weak correlations appear by chance and not weighty, although this dependence was reported for radio sources in several studies (e.g. Blumenthal & Miley 1979; Laing & Peacock 1980; De Breuck et al. 2000). The result does not contradict the existing theories, explaining $z\text{--}\alpha$ correlation by the interaction of the radio lobes with the dense intergalactic medium at $z \sim 2\text{--}3$. Our sample contains distant ($z > 3$) and very compact radio sources, mostly with peaked radio spectra, for which the core emission dominates at the GHz frequencies and the influence of radio lobes is negligible (Ker et al. 2012).

4.5 Radio luminosity

We used the Λ CDM cosmology with $H_0 = 67.74 \text{ km s}^{-1} \text{ Mpc}^{-1}$, $\Omega_m = 0.3089$, and $\Omega_\Lambda = 0.6911$ (Planck Collaboration 2016) to estimate the radio luminosity at 4.7 GHz:

$$L_\nu = 4\pi D_L^2 \nu S_\nu (1+z)^{-\alpha-1}, \quad (2)$$

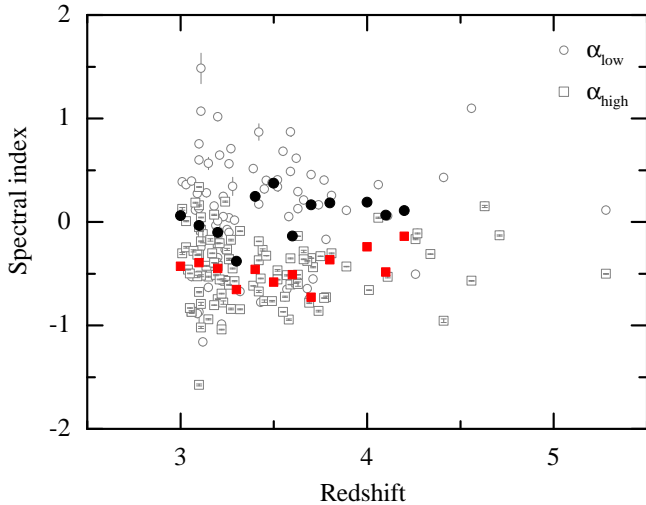


Figure 8. α versus z plot for low and high frequencies. The filled symbols represent the median values of the spectral indices for redshift bins of 0.1, from 3.0 to 4.2.

where ν is the frequency, S_ν the measured flux density, z the redshift, α the spectral index calculated at 4.7 GHz by linear approximation of the spectrum between 1 and 8 GHz, and D_L the luminosity distance.

The median value of the radio luminosity for our sample is $\sim 2 \times 10^{44}$ erg s $^{-1}$, and the source J0525–3343 at $z = 4.41$ has the highest luminosity of 3.38×10^{45} erg s $^{-1}$. Figs 9 and 10 show the luminosity distribution and the redshift versus luminosity plot, respectively.

In Fig. 10 we compare the luminosities of our sample with the luminosities calculated for the 17 distant quasars at $z > 5.5$ selected from the FIRST and Pan-STARRS1 surveys cross-match in Bañados et al. (2015). Also, we draw in the figure five individual sources: BZQ J0906+6930 at $z = 5.47$, PSO J047.4478+27.2992 at $z = 6.1$ and NVSS J164854+460328 at $z = 5.38$ (Mufakharov et al. 2021), VIK J2318-3113 at $z = 6.44$ (Ighina et al. 2021), and PSO J172.3556+18.7734 at $z = 6.82$ (Bañados et al. 2021). The sample of Bañados et al. (2015) consists of the sources with the 1.4 GHz flux densities in the range 0.035–3.04 mJy, and accordingly their luminosity values are two orders of magnitude lower compared to the values in our sample.

4.6 Radio loudness

The radio loudness is defined as

$$R = \frac{S_{\nu,\text{radio}}}{S_{\nu,\text{opt}}} \quad (3)$$

where $S_{\nu,\text{radio}}$ is the estimated radio flux density at 4.7 GHz and $S_{\nu,\text{opt}}$ is the optical flux density corresponding to the filter B or g .

Optical data were taken from the SIMBAD database,⁴ where B or g magnitudes are presented for 71 of 102 objects. The magnitudes were transformed into flux densities using the Pogson law. We adopted $S_{\nu,\text{opt}} = 3631$ Jy for g

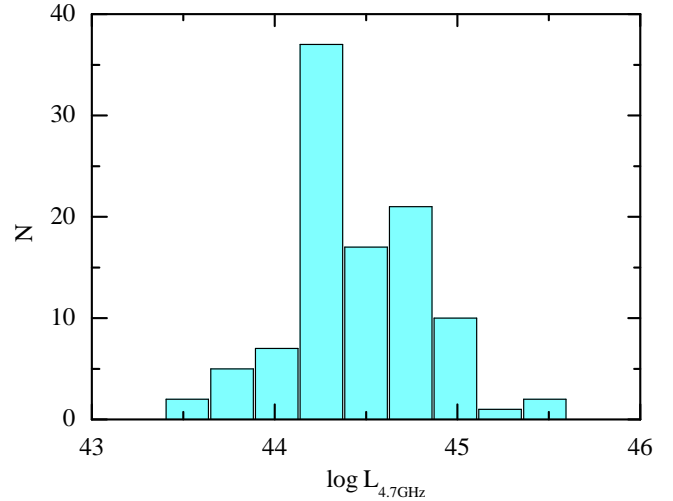


Figure 9. Radio luminosity distribution.

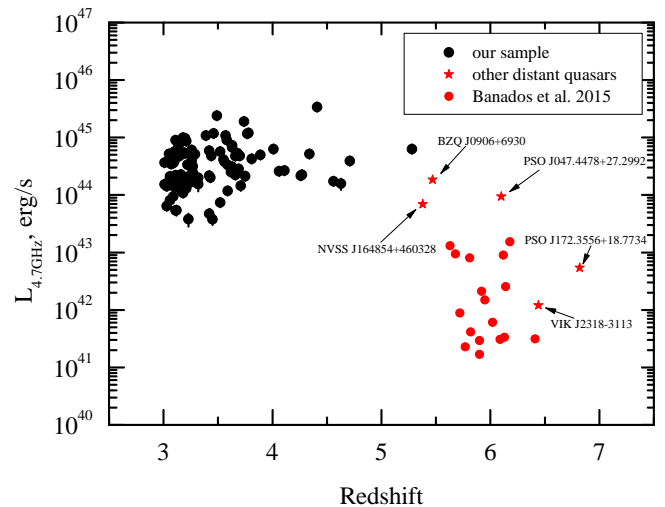


Figure 10. Redshift versus luminosity. The sample of distant blazars from Bañados et al. (2015) is shown with the red circles and other five distant quasars from the literature are marked with the red stars.

$= 0$,⁵, $S_{\nu,\text{opt}} = 4260$ Jy for $B = 0$ (Bessell 1979), and the optical spectral index $\alpha = -0.3$ (Ganci et al. 2019).

Fig. 11 presents the radio loudness distribution. The log R value spans from 2.1 to 5.43, the median is 3.5, and the majority of the sources are highly radio loud with log $R > 2.5$ (Zhu et al. 2019). Only 5 of 71 quasars have log $R < 2.5$.

In Fig. 12 we draw 24 radio-loud blazars at $z > 4$ selected from the Cosmic Lens All Sky Survey (CLASS: Ighina et al. 2019) as well as five individual sources - BZQ J0906+6930 at $z = 5.47$ (Romani et al. 2004), PSO J352.4034-15.3373 at $z = 5.84$ (Bañados et al. 2018), PSO J047.4478+27.2992 at $z = 6.1$ (Belladitta et al. 2020), VIK J2318-3113 at $z = 6.44$ (Ighina et al. 2021), and PSO J172.3556+18.7734 at $z = 6.82$ (Bañados et al. 2021), - to compare with our results. The sample of Ighina et al. (2019) was selected with a lower

⁴ <https://simbad.u-strasbg.fr/simbad/>

⁵ <https://www.sdss.org/dr12/algorithms/fluxcal/#SDSStoAB>

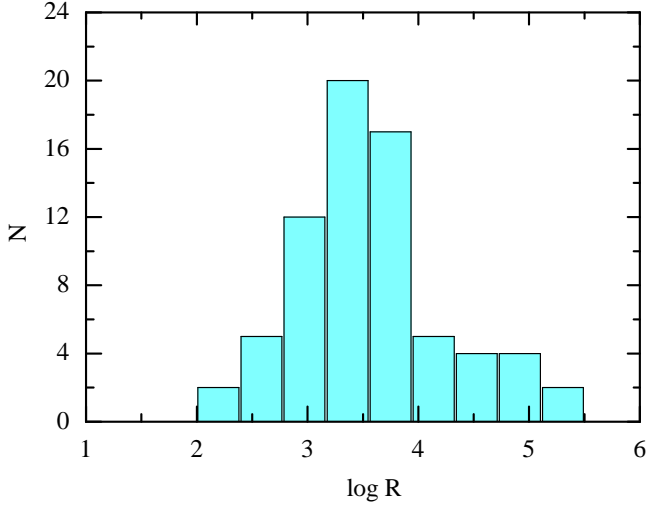


Figure 11. Radio loudness distribution.

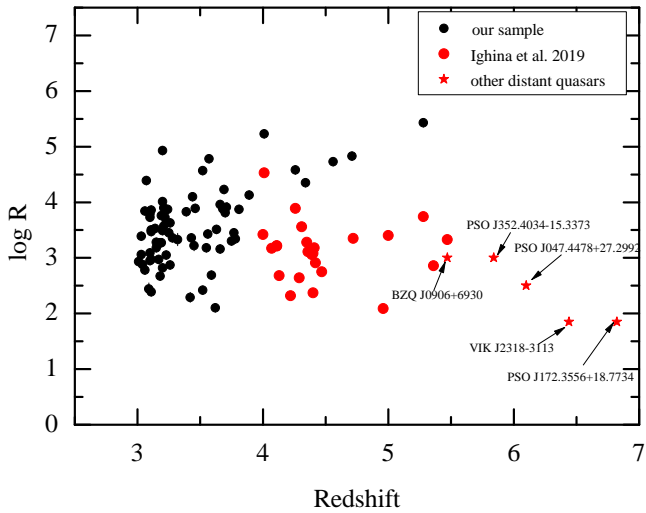


Figure 12. Redshift versus radio loudness. The sample of distant blazars from Ighina et al. (2019) is shown with the red circles, and other five distant quasars from the literature are marked with the red stars.

limit of 30 mJy at 1.4 GHz, therefore it contains fainter radio sources with lower radio-loudness values than our sample, which is reflected in Fig. 12. We also discuss selection effects in the following section.

5 DISCUSSION

We have classified 46 per cent spectra of $z \geq 3$ quasars as PS type, which is quite a large fraction of bright distant quasars. Thus, we confirm the earlier result of O’Dea et al. (1990) who revealed that seven of the 14 quasars studied at $z \geq 3$ are GPS. Also, O’Dea (1998) expects about 40 per cent of all bright radio sources to be PS type (GPS and CSS).

If a PS source has a peak between 0.5 and 10 GHz, then it is classified as GPS; however, if the spectrum has a peak around 1 GHz, the spectral indices of the optically thin and thick parts are about 0.51 and -0.73 , and the source is non-

variable, then it is classified more precisely as a classical or canonical GPS (de Vries et al. 1997). In our sample, 17 sources (17 per cent) fit the criteria of classical GPS. 12 of them are already known as GPS or MPS in de Vries et al. (1997), O’Dea (1998), and Callingham et al. (2017). For the other five, further study of their variability (Sotnikova 2021, in preparation) will help classify them more precisely. The variability is a crucial parameter when distinguishing between PS quasars and classical GPS (O’Dea & Saikia 2020).

Several studies (Torniainen et al. 2005; Mingaliev et al. 2012, 2013; Sotnikova et al. 2019a) have shown that only 2–3 per cent of PS objects are classical GPS, whereas other GPS sources could be, in fact, the blazars that temporarily have broader peaked spectra during their flares (Planck Collaboration et al. 2011). 50 per cent of PS objects in the sample (24 of 47) are FSRQs.

We compared the spectra of GPS quasars in the samples from Mingaliev et al. (2012, 2013) and Sotnikova et al. (2019a). There is no difference between averaged optically thick and thin spectral indices within the measurement uncertainties (Table 4). This can mean that the high redshift GPS have, on average, the same spectral indices as the low- and medium-redshift GPS, and there is no evidence for the evolution of the radio spectrum.

Among 47 PS objects, we determined that 13 (13 per cent) MPSs in the sample that are the sources with a peak below 1 GHz in the observer’s frame. They are also interesting as young compact (5–10 mas) radio sources (Coppejans et al. 2015, 2016a; Callingham et al. 2017), possibly evolved versions of GPS sources (Kunert-Bajraszewska et al. 2010). On the whole, MPS sources are a combination of PS sources, the peak frequency of which have been shifted to low frequencies due to cosmological redshift (O’Dea & Saikia 2021). Two of our 13 MPSs had already been identified as MPSs in Callingham et al. (2017). We note that 15 objects of the sample with the steep spectrum could also be MPS candidates, and additional low-frequency (<1 GHz) data are needed to obtain their radio spectra at megahertz frequencies and define a possible peak.

Whitfield (1957), Blumenthal & Miley (1979), Tielens et al. (1979), Laing & Peacock (1980), De Breuck et al. (2000), Jarvis et al. (2001), Verkhodanov & Khabibullina (2010), and Singh et al. (2014) reported a correlation between the observed spectral index and redshift and also proposed to use the presence of an ultra-steep spectral index as a method for selecting high-redshift radio sources. However, this correlation was detected mostly for radio galaxies, while more and more distant quasars with flat radio spectra have been revealed later. The steeper spectra for distant quasars could be explained by selection effects and higher inverse Compton losses due to the increased photon energy density of the cosmic microwave background (Morabito & Harwood 2018). We have no quasars with the ultra-steep spectrum in the sample.

The number of objects in our sample decreases with increasing redshift, whereas the radio loudness increases. This means that our initial criterion of $S_{1.4} \geq 100$ mJy selects only the most radio-loud quasars at high redshifts. There are other radio-loud quasars underrepresented in our study because of their low radio flux density at $\nu_{\text{obs}} = 1.4$ GHz. The quasar radio-loud fraction was investigated in several studies, and it was shown that it remains about ~ 10 per cent in optically selected quasar samples up to redshift $z \sim 6$ (Kellermann

et al. 1989; Stern et al. 2000; Liu et al. 2021). When higher redshifts are considered, the lower-frequency observations are needed to detect the radio emission because of the steep spectrum at MHz–GHz frequencies. We think that the artificial trend we obtained in the $\log R$ – z plane will be eliminated if the selection criterion is changed toward a lower flux density limit at 1.4 GHz, or if a lower frequency survey is applied to the high-redshift sample construction.

6 SUMMARY

We present the results of multifrequency RATAN observations in 2017–2020 of a complete sample of bright quasars at $z \geq 3$. The flux densities were measured at frequencies of 1.1, 2.3, 4.7, 8.2, 11.2, and 22 GHz quasi-simultaneously with uncertainties of 9–31 per cent. The detection rate is 100, 89, and 46 per cent at 4.7, 11.2, and 22 GHz, respectively. The main conclusions are the following:

(i) The sample has peaked and flat radio spectra (46 per cent and 24 per cent, respectively). There are 15 per cent quasars with a steep spectrum ($-1.1 < \alpha < -0.5$), indicating the dominance of bright compact core emission and insignificant contribution of extended optically thin kpc-scale components in observed radio spectra. There are no quasars with ultra-steep radio spectra ($\alpha \leq -1.1$) in the sample. We have not found any significant correlation between the redshifts and spectral indices.

(ii) Eight new MPSs (J0214+0157, J0232+2317, J0525–3343, J0624+3856, J0905+0410, J1045+3142, J1418+4250, J2019+1127) and 16 new GPS (Table 2) candidates are suggested. Further study of their variability and additional low-frequency observations are needed to classify them precisely.

(iii) The radio luminosity $L_{4.7}$ has been calculated with a median value of $\sim 2 \times 10^{44}$ erg s $^{-1}$ for the sample.

(iv) Using new radio data, we have estimated the radio loudness for 71 objects with a mean value of 3.5. The $\log R$ values span from 2.1 to 5.43. The majority of the quasars are highly radio-loud with $\log R > 2.5$, and only five quasars have $\log R < 2.5$.

We are preparing a follow-up work with a further study of the sample, including assessing the variability and notes on individual objects (Sotnikova, in preparation).

ACKNOWLEDGEMENTS

We thank the referee for providing useful suggestions and comments that significantly improved the article. This work was supported in the framework of the national project “Science” by the Ministry of Science and Higher Education of the Russian Federation under the contract 075-15-2020-778. The observations were carried out with the RATAN-600 scientific facility. This research has made use of the CATS database, operated at SAO RAS, Russia. The research has made use of the NASA/IPAC Extragalactic Database (NED), which is operated by the Jet Propulsion Laboratory, California Institute of Technology, under contract with the National Aeronautics and Space Administration. We used of the SIMBAD database, operated at CDS, Strasbourg, France.

DATA AVAILABILITY

The data underlying this article are available in the article and in its online supplementary material. The measured flux densities are distributed in the VizieR Information System and partly published in the BL Lac database available at the Special Astrophysical Observatory website.

REFERENCES

- Bañados E., et al., 2015, *ApJ*, 804, 118
 Bañados E., Carilli C., Walter F., Momjian E., Decarli R., Farina E. P., Mazzucchelli C., Venemans B. P., 2018, *ApJ*, 861, L14
 Bañados E., et al., 2021, *ApJ*, 909, 80
 Baars J. W. M., Genzel R., Pauliny-Toth I. I. K., Witzel A., 1977, *A&A*, 61, 99
 Ballet J., Burnett T. H., Digel S. W., Lott B., 2020, arXiv e-prints, p. arXiv:2005.11208
 Becker R. H., White R. L., Helfand D. J., 1994, in Crabtree D. R., Hanisch R. J., Barnes J., eds, *Astronomical Society of the Pacific Conference Series Vol. 61, Astronomical Data Analysis Software and Systems III*. p. 165
 Belladitta S., et al., 2020, *A&A*, 635, L7
 Bessell M. S., 1979, *PASP*, 91, 589
 Blumenthal G., Miley G., 1979, *A&A*, 80, 13
 Caccianiga A., et al., 2019, *MNRAS*, 484, 204
 Callingham J. R., et al., 2017, *ApJ*, 836, 174
 Condon J. J., Cotton W. D., Greisen E. W., Yin Q. F., Perley R. A., Taylor G. B., Broderick J. J., 1998, *AJ*, 115, 1693
 Coppejans R., Cseh D., Williams W. L., van Velzen S., Falcke H., 2015, *MNRAS*, 450, 1477
 Coppejans R., et al., 2016a, *MNRAS*, 459, 2455
 Coppejans R., et al., 2016b, *MNRAS*, 463, 3260
 Coppejans R., et al., 2017, *MNRAS*, 467, 2039
 De Breuck C., van Breugel W., Röttgering H. J. A., Miley G., 2000, *A&AS*, 143, 303
 Frey S., Gurvits L. I., Paragi Z., É. Gabányi K., 2008, *A&A*, 484, L39
 Frey S., Paragi Z., Gurvits L. I., Cseh D., Gabányi K. É., 2010, *A&A*, 524, A83
 Frey S., Paragi Z., Fogasy J. O., Gurvits L. I., 2015, *MNRAS*, 446, 2921
 Ganci V., Marziani P., D’Onofrio M., del Olmo A., Bon E., Bon N., Negrete C. A., 2019, *A&A*, 630, A110
 Ghisellini G., Sbarrato T., Tagliaferri G., Foschini L., Tavecchio F., Ghirlanda G., Braito V., Gehrels N., 2014, *MNRAS*, 440, L111
 Gregory P. C., Scott W. K., Douglas K., Condon J. J., 1996, *ApJS*, 103, 427
 Hurley-Walker N., et al., 2017, *MNRAS*, 464, 1146
 Ighina L., Caccianiga A., Moretti A., Belladitta S., Della Ceca R., Ballo L., Dallacasa D., 2019, *MNRAS*, 489, 2732
 Ighina L., Belladitta S., Caccianiga A., Broderick J. W., Drouart G., Moretti A., Seymour N., 2021, arXiv e-prints, p. arXiv:2101.11371
 Intema H. T., Jagannathan P., Mooley K. P., Frail D. A., 2017, *A&A*, 598, A78
 Jarvis M. J., et al., 2001, *MNRAS*, 326, 1563
 Kellermann K. I., Sramek R., Schmidt M., Shaffer D. B., Green R., 1989, *AJ*, 98, 1195
 Ker L. M., Best P. N., Rigby E. E., Röttgering H. J. A., Gendre M. A., 2012, *MNRAS*, 420, 2644
 Kovalev Y. Y., Kovalev Y. A., Nizhelsky N. A., Bogdantsov A. B., 2002, *Publications of the Astronomical Society of Australia*, 19, 83
 Kovalev Y. A., et al., 2020, *Advances in Space Research*, 65, 745

Table 4. Comparison of spectral indices of quasars with the classical GPS features in different samples: α_{below} and α_{above} are the median spectral indices below and above the turnover, respectively.

z	N	α_{below}	α_{above}	Reference
0.14–4.56	45	0.7 (0.1)	−0.7 (0.1)	Mingaliev et al. (2012)
0–5	43	0.9 (0.1)	−0.6 (0.1)	Mingaliev et al. (2013)
				$S_5 \geq 0.2$ Jy
0–5	71	0.7 (0.2)	−0.7 (0.2)	Sotnikova et al. (2019a)
				$S_5 \geq 0.2$ Jy
3–5	12	0.7 (0.2)	−0.7 (0.3)	This study
				$S_{1.4} \geq 0.1$ Jy

- Kunert-Bajraszewska M., Gawroński M. P., Labiano A., Siemiginowska A., 2010, *MNRAS*, 408, 2261
- Laing R. A., Peacock J. A., 1980, *MNRAS*, 190, 903
- Liu Y., et al., 2021, *ApJ*, 908, 124
- Marecki A., Falcke H., Niezgoda J., Garrington S. T., Patnaik A. R., 1999, *A&AS*, 135, 273
- Massaro E., Maselli A., Leto C., Marchegiani P., Perri M., Giommi P., Piranomonte S., 2015, *Ap&SS*, 357, 75
- Mingaliev M. G., Stolyarov V. A., Davies R. D., Melhuish S. J., Bursov N. A., Zhekanis G. V., 2001, *A&A*, 370, 78
- Mingaliev M. G., Sotnikova Y. V., Torniainen I., Tornikoski M., Udovitskiy R. Y., 2012, *A&A*, 544, A25
- Mingaliev M. G., Sotnikova Y. V., Mufakharov T. V., Erkenov A. K., Udovitskiy R. Y., 2013, *Astrophysical Bulletin*, 68, 262
- Mingaliev M. G., Sotnikova Y. V., Udovitskiy R. Y., Mufakharov T. V., Nieppola E., Erkenov A. K., 2014, *A&A*, 572, A59
- Momjian E., Carilli C. L., McGreer I. D., 2008, *AJ*, 136, 344
- Momjian E., Carilli C. L., Walter F., Venemans B., 2014, *AJ*, 147, 6
- Morabito L. K., Harwood J. J., 2018, *MNRAS*, 480, 2726
- Mufakharov T., Mikhailov A., Sotnikova Y., Mingaliev M., Stolyarov V., Erkenov A., Nizhelskij N., Tsybulev P., 2021, *MNRAS*, 503, 4662
- Murphy T., et al., 2010, *MNRAS*, 402, 2403
- O’Dea C. P., 1990, *MNRAS*, 245, 20
- O’Dea C. P., 1998, *PASP*, 110, 493
- O’Dea C. P., Saikia D. J., 2020, arXiv e-prints, p. arXiv:2009.02750
- O’Dea C. P., Saikia D. J., 2021, *A&ARv*, 29, 3
- O’Dea C. P., Baum S. A., Stanghellini C., Morris G. B., Patnaik A. R., Gopal-Krishna 1990, *A&AS*, 84, 549
- O’Dea C. P., Baum S. A., Stanghellini C., 1991, *ApJ*, 380, 66
- Ott M., Witzel A., Quirrenbach A., Krichbaum T. P., Standke K. J., Schalinski C. J., Hummel C. A., 1994, *A&A*, 284, 331
- Parijskij Y. N., 1993, *IEEE Antennas and Propagation Magazine*, 35, 7
- Perley R. A., Butler B. J., 2013, *ApJS*, 204, 19
- Perley R. A., Butler B. J., 2017, *ApJS*, 230, 7
- Planck Collaboration 2016, *A&A*, 594, A13
- Planck Collaboration et al., 2011, *A&A*, 536, A14
- Rengelink R. B., Tang Y., de Bruyn A. G., Miley G. K., Bremer M. N., Roettgering H. J. A., Bremer M. A. R., 1997, *A&AS*, 124, 259
- Romani R. W., Sowards-Emmerd D., Greenhill L., Michelson P., 2004, *ApJ*, 610, L9
- Sbarrato T., et al., 2012, *MNRAS*, 426, L91
- Sbarrato T., Ghisellini G., Nardini M., Tagliaferri G., Greiner J., Rau A., Schady P., 2013, *MNRAS*, 433, 2182
- Singh V., et al., 2014, *A&A*, 569, A52
- Slish V. I., 1963, *Nature*, 199, 682
- Smolčić V., et al., 2014, *MNRAS*, 443, 2590
- Sotnikova Y. V., 2020, in Romanyuk I. I., Yakunin I. A., Valeev A. F., Kudryavtsev D. O., eds, *Ground-Based Astronomy in Russia. 21st Century*. pp 32–40, doi:10.26119/978-5-6045062-0-2’2020’32
- Sotnikova Y. V., Mufakharov T. V., Majorova E. K., Mingaliev M. G., Udovitskii R. Y., Bursov N. N., Semenova T. A., 2019a, *Astrophysical Bulletin*, 74, 348
- Sotnikova Y. V., Kovalev Y. A., Erkenov A. K., 2019b, *Astrophysical Bulletin*, 74, 497
- Spingola C., Dallacasa D., Belladitta S., Caccianiga A., Giroletti M., Moretti A., Orienti M., 2020, *A&A*, 643, L12
- Stern D., Djorgovski S. G., Perley R. A., de Carvalho R. R., Wall J. V., 2000, *AJ*, 119, 1526
- Tabara H., Inoue M., 1980, *A&AS*, 39, 379
- Tielens A. G. G. M., Miley G. K., Willis A. G., 1979, *A&AS*, 35, 153
- Torniainen I., Tornikoski M., Teräsanta H., Aller M. F., Aller H. D., 2005, *A&A*, 435, 839
- Tsybulev P. G., 2011, *Astrophysical Bulletin*, 66, 109
- Tsybulev P. G., Nizhelskii N. A., Dugin M. V., Borisov A. N., Kratov D. V., Udovitskii R. Y., 2018, *Astrophysical Bulletin*, 73, 494
- Udovitskiy R. Y., Sotnikova Y. V., Mingaliev M. G., Tsybulev P. G., Zhekanis G. V., Nizhelskij N. A., 2016, *Astrophysical Bulletin*, 71, 496
- Urry C. M., Padovani P., 1995, *PASP*, 107, 803
- Verkhodanov O. V., 1997, *Astronomical Data Analysis Software and Systems VI*, A.S.P. Conference Series, 125, 46
- Verkhodanov O. V., Khabibullina M. L., 2010, *Astronomy Letters*, 36, 7
- Verkhodanov O. V., Trushkin S. A., Chernenkov V. N., 1997, *Baltic Astronomy*, 6, 275
- Verkhodanov O. V., Trushkin S. A., Andernach H., Chernenkov V. N., 2005, *Bulletin of the Special Astrophysics Observatory*, 58, 118
- Verkhodanov O. V., Kozlova D. D., Sotnikova Y. V., 2018, *Astrophysical Bulletin*, 73, 393
- Wang R., et al., 2007, *AJ*, 134, 617
- Whitfield G. R., 1957, *MNRAS*, 117, 680
- Zhu S. F., Brandt W. N., Wu J., Garmire G. P., Miller B. P., 2019, *MNRAS*, 482, 2016
- de Vries W. H., Barthel P. D., O’Dea C. P., 1997, *A&A*, 321, 105

Table 1: The sample parameters: source name, redshift z , average flux density $S_{4.7}$ and radio luminosity $L_{4.7}$, spectral indices α_{low} and α_{high} , radio-loudness $\log R$, radio-spectrum type, and blazar type. The redshifts are taken from the NED database, and other parameters presented in Columns 3–8 are estimations based on RATAN-600 measurements.

NVSS name	z	$S_{4.7}$, (Jy)	$L_{4.7} \times 10^{44}$, (erg s $^{-1}$)	$\log R$	α_{low}	α_{high}	Sp. type	Blazar type
1	2	3	4	5	6	7	8	9
000108+191434	3.10	0.15 ± 0.01	1.38 ± 0.17		-0.87 ± 0.11	+0.16 ± 0.01	upturn	FSRQ
000657+141546	3.20	0.14 ± 0.01	1.27 ± 0.13	2.82 ± 0.04	+0.02 ± 0.02	-0.21 ± 0.01	peaked	
004858+064005	3.58	0.17 ± 0.01	9.07 ± 1.13		+0.05 ± 0.03	-0.95 ± 0.01	peaked	
010012-270852	3.52	0.12 ± 0.01	0.74 ± 0.11	2.42 ± 0.05	+0.41 ± 0.04	-0.47 ± 0.01	peaked	
012100-280622	3.11	0.17 ± 0.01	1.74 ± 0.12		+1.45 ± 0.15	-0.08 ± 0.01	peaked	FSRQ
013113+435813	3.12	0.03 ± 0.01	0.54 ± 0.10		-1.16 ± 0.02	-0.12 ± 0.08	complex	
014844+421519	3.24	0.11 ± 0.01	1.68 ± 0.20		-0.27 ± 0.02	+0.20 ± 0.01	upturn	FSRQ
015106+251729	3.10	0.13 ± 0.01	1.41 ± 0.12	3.73 ± 0.03	-0.05 ± 0.01	-0.05 ± 0.01	flat	
020346+113445	3.63	0.65 ± 0.03	7.30 ± 0.69	3.51 ± 0.04	+0.29 ± 0.01	-0.51 ± 0.01	peaked*	FSRQ
021435+015703	3.28	0.08 ± 0.01	1.71 ± 0.22	3.36 ± 0.06	+0.34 ± 0.09	-0.45 ± 0.01	peaked	
023220+231757	3.42	0.31 ± 0.02	5.86 ± 0.64		+0.87 ± 0.08	-0.37 ± 0.01	peaked*	
024611+182330	3.59	0.17 ± 0.01	3.32 ± 0.24		+0.49 ± 0.02	-0.35 ± 0.01	peaked	FSRQ
025759+433838	4.06	0.31 ± 0.02	2.59 ± 0.25		+0.36 ± 0.01	+0.04 ± 0.01	inverted	
032444-291821	4.63	0.15 ± 0.01	1.58 ± 0.35		+0.15 ± 0.01	+0.15 ± 0.01	inverted	FSRQ
033755-120404	3.44	0.29 ± 0.02	4.79 ± 0.42	4.10 ± 0.04	-0.32 ± 0.01	-0.27 ± 0.01	flat	FSRQ
033900-013318	3.19	0.37 ± 0.02	5.43 ± 0.49	3.76 ± 0.04	-0.03 ± 0.01	-0.40 ± 0.01	flat	FSRQ
035424+044107	3.26	0.39 ± 0.02	3.97 ± 0.38		+0.04 ± 0.02	-0.36 ± 0.01	complex	
042457+080517	3.09	0.19 ± 0.01	1.59 ± 0.16		+0.11 ± 0.02	+0.19 ± 0.01	inverted	FSRQ
042835+173223	3.32	0.15 ± 0.01	1.98 ± 0.13		-0.09 ± 0.01	-0.09 ± 0.01	flat	FSRQ
052506-233810	3.1	0.74 ± 0.03	3.85 ± 0.38	3.09 ± 0.04	+0.60 ± 0.01	+0.34 ± 0.01	inverted	bl.un.
052506-334305	4.41	0.40 ± 0.01	33.80 ± 4.45		+0.43 ± 0.02	-0.96 ± 0.02	peaked	FSRQ
053954-283955	3.10	0.99 ± 0.10	5.65 ± 0.56	3.79 ± 0.04	+0.32 ± 0.01	-0.32 ± 0.01	peaked*	FSRQ
062419+385648	3.46	0.61 ± 0.03	11.80 ± 1.18	3.89 ± 0.04	+0.40 ± 0.01	-0.33 ± 0.01	peaked	FSRQ
064632+445116	3.39	2.27 ± 0.10	10.80 ± 1.00	3.83 ± 0.04	+0.52 ± 0.01	-0.62 ± 0.01	peaked	FSRQ
073357+045614	3.01	0.53 ± 0.03	3.66 ± 0.37		+0.39 ± 0.01	-0.31 ± 0.01	peaked	FSRQ
075141+271632	3.20	0.20 ± 0.01	5.29 ± 0.62	4.93 ± 0.05	+1.02 ± 0.03	-0.75 ± 0.01	peaked	
075303+423131	3.59	0.41 ± 0.02	1.18 ± 0.17	2.69 ± 0.05	+0.87 ± 0.04	-0.61 ± 0.01	peaked	
083322+095941	3.75	0.09 ± 0.01	2.12 ± 0.23	3.30 ± 0.05	-0.33 ± 0.01	-0.33 ± 0.01	flat	
083910+200207	3.03	0.12 ± 0.01	0.64 ± 0.07	3.06 ± 0.04	+0.36 ± 0.01	-0.25 ± 0.01	peaked	
084715+383110	3.18	0.11 ± 0.01	1.08 ± 0.10	2.67 ± 0.04	+0.07 ± 0.01	+0.07 ± 0.01	inverted	
090549+041010	3.15	0.09 ± 0.01	1.98 ± 0.23	3.28 ± 0.05	+0.57 ± 0.06	-0.53 ± 0.01	peaked	
090915+035443	3.20	0.13 ± 0.01	1.61 ± 0.14	3.49 ± 0.04	-0.35 ± 0.01	-0.10 ± 0.01	flat	
091551+000712	3.07	0.21 ± 0.01	3.44 ± 0.35	4.39 ± 0.05	-0.28 ± 0.01	-0.28 ± 0.01	flat	FSRQ
093337+284532	3.42	0.05 ± 0.01	0.47 ± 0.01	2.29 ± 0.09	+0.17 ± 0.02	-0.67 ± 0.01	peaked	
094113+114532	3.19	0.12 ± 0.01	1.94 ± 0.23	3.27 ± 0.05	-0.51 ± 0.01	-0.51 ± 0.01	flat	
101644+203747	3.11	0.55 ± 0.03	8.93 ± 0.79	3.86 ± 0.04	-0.07 ± 0.01	-0.52 ± 0.01	complex	FSRQ
102010+104003	3.15	0.15 ± 0.01	4.77 ± 0.40	3.18 ± 0.04	-0.63 ± 0.01	-0.94 ± 0.01	steep	
102107+220922	4.26	0.12 ± 0.01	2.17 ± 0.23	4.58 ± 0.05	-0.51 ± 0.01	-0.17 ± 0.01	flat	
102623+254259	5.28	0.11 ± 0.01	6.31 ± 0.60	5.43 ± 0.04	+0.11 ± 0.03	-0.50 ± 0.01	peaked	FSRQ
102645+365826	3.25	0.19 ± 0.01	2.25 ± 0.19	3.45 ± 0.03	-0.08 ± 0.01	-0.27 ± 0.01	flat	
102838-084438	4.27	0.10 ± 0.01	2.25 ± 0.21		-0.11 ± 0.01	-0.11 ± 0.01	flat	FSRQ
103626+132652	3.09	0.04 ± 0.01	0.94 ± 0.22	2.44 ± 0.11	-0.89 ± 0.01	-0.53 ± 0.01	steep	
104523+314232	3.23	0.08 ± 0.01	1.72 ± 0.25	3.05 ± 0.06	+0.25 ± 0.03	-0.56 ± 0.01	peaked	
110147+001039	3.69	0.06 ± 0.01	2.84 ± 0.46	4.23 ± 0.07	-0.74 ± 0.01	-0.78 ± 0.01	steep	
112500+333858	3.43	0.08 ± 0.01	2.01 ± 0.27	3.36 ± 0.06	-0.78 ± 0.01	-0.55 ± 0.01	steep	
112851+232617	3.04	0.10 ± 0.01	1.63 ± 0.18	2.88 ± 0.05	-0.46 ± 0.01	-0.46 ± 0.01	flat	
115016+433205	3.03	0.11 ± 0.01	1.42 ± 0.10	3.39 ± 0.03	+0.01 ± 0.01	+0.01 ± 0.01	inverted	FSRQ
123055-113909	3.52	0.18 ± 0.01	5.67 ± 0.59	4.57 ± 0.05	+0.34 ± 0.04	-0.56 ± 0.01	peaked	FSRQ
124209+372006	3.81	0.56 ± 0.02	4.23 ± 0.43	3.87 ± 0.04	+0.26 ± 0.01	-0.30 ± 0.01	peaked*	
130122+190353	3.10	0.08 ± 0.01	1.63 ± 0.26		+0.13 ± 0.01	-0.68 ± 0.01	peaked	
134022+375443	3.11	0.30 ± 0.02	0.54 ± 0.05	2.39 ± 0.04	+1.07 ± 0.01	-1.02 ± 0.01	peaked	
135406-020603	3.70	0.70 ± 0.04	4.80 ± 0.49	3.81 ± 0.04	+0.46 ± 0.01	-0.35 ± 0.01	peaked	FSRQ
135646-110130	3.01	0.23 ± 0.01	1.53 ± 0.18	2.93 ± 0.05	+0.13 ± 0.01	+0.13 ± 0.01	inverted	FSRQ
135652+291817	3.24	0.05 ± 0.01	1.63 ± 0.25	3.87 ± 0.07	-0.57 ± 0.01	-0.57 ± 0.01	steep	
135706-174402	3.14	0.65 ± 0.04	7.20 ± 0.75	3.53 ± 0.04	+0.28 ± 0.01	-0.42 ± 0.01	peaked*	FSRQ
140135+151326	3.23	0.04 ± 0.01	0.38 ± 0.10	3.63 ± 0.12	+0.05 ± 0.01	-0.78 ± 0.02	peaked	
140501+041535	3.20	0.73 ± 0.03	9.65 ± 0.89	4.01 ± 0.04	+0.01 ± 0.01	-0.43 ± 0.01	peaked*	FSRQ
141152+430024	3.21	0.09 ± 0.01	1.30 ± 0.14	3.57 ± 0.05	-0.21 ± 0.01	-0.21 ± 0.01	flat	
141300+394745	3.71	0.05 ± 0.01	1.44 ± 0.27	3.91 ± 0.08	-0.55 ± 0.01	-0.44 ± 0.01	flat	
141318+450522	3.11	0.16 ± 0.01	1.40 ± 0.10	3.47 ± 0.03	+0.04 ± 0.01	+0.04 ± 0.01	inverted	FSRQ

Table 1: continued.

NVSS name	z	$S_{4.7}$, (Jy)	$L_{4.7} \times 10^{44}$, (erg s $^{-1}$)	$\log R$	α_{low}	α_{high}	Sp. type	Blazar type
1	2	3	4	5	6	7	8	9
141821+425020	3.45	0.05 ± 0.01	0.38 ± 0.08	3.22 ± 0.09	+0.32 ± 0.01	-0.77 ± 0.01	peaked	
142107-064356	3.68	0.22 ± 0.01	5.33 ± 0.52	3.88 ± 0.04	-0.65 ± 0.01	-0.38 ± 0.01	complex	FSRQ
142438+225600	3.62	0.61 ± 0.03	2.52 ± 0.28	2.10 ± 0.05	+0.62 ± 0.01	-0.59 ± 0.01	peaked	FSRQ
143023+420436	4.71	0.12 ± 0.01	3.88 ± 0.27	4.83 ± 0.03	-0.13 ± 0.01	-0.13 ± 0.01	flat	FSRQ
144516+095836	3.55	0.98 ± 0.04	4.12 ± 0.43	3.18 ± 0.04	+0.68 ± 0.01	-0.87 ± 0.01	peaked	FSRQ
145722+051922	3.17	0.07 ± 0.01	1.16 ± 0.16	2.97 ± 0.06	-0.30 ± 0.01	-0.30 ± 0.01	flat	
145805+085529	3.06	0.06 ± 0.01	2.10 ± 0.35	3.84 ± 0.07	-0.53 ± 0.01	-0.87 ± 0.01	steep	
145927+325359	3.32	0.05 ± 0.01	1.54 ± 0.39	3.33 ± 0.11	-0.67 ± 0.01	-0.85 ± 0.01	steep	
150328+041949	3.66	0.19 ± 0.01	2.23 ± 0.15	3.16 ± 0.03	+0.21 ± 0.01	-0.29 ± 0.01	peaked	
152117+175601	3.06	0.13 ± 0.01	0.81 ± 0.08	2.78 ± 0.04	+0.40 ± 0.03	-0.87 ± 0.01	peaked	
152219+211957	3.22	0.08 ± 0.01	3.35 ± 0.48	3.73 ± 0.06	-0.99 ± 0.01	-1.04 ± 0.01	steep	
153815+001905	3.49	0.32 ± 0.02	24.00 ± 2.50		+0.38 ± 0.01	-0.77 ± 0.01	peaked	
155930+030447	3.89	0.43 ± 0.02	4.97 ± 0.50	4.13 ± 0.04	+0.11 ± 0.01	-0.43 ± 0.01	peaked	FSRQ
160002+041256	3.11	0.16 ± 0.01	2.07 ± 0.14	3.50 ± 0.03	-0.19 ± 0.01	-0.19 ± 0.01	flat	
160608+312504	4.56	0.64 ± 0.03	1.73 ± 0.22	4.73 ± 0.05	+1.10 ± 0.02	-0.57 ± 0.01	peaked	
161005+181143	3.11	0.07 ± 0.01	2.20 ± 0.35	2.97 ± 0.06	-0.25 ± 0.01	-0.79 ± 0.02	steep	
161637+045932	3.21	1.03 ± 0.04	8.63 ± 0.80	3.90 ± 0.04	+0.64 ± 0.01	-0.56 ± 0.01	peaked*	FSRQ
163257-003321	3.42	0.15 ± 0.01	2.17 ± 0.16		-0.19 ± 0.01	-0.19 ± 0.01	flat	FSRQ
165519+324241	3.18	0.06 ± 0.01	2.06 ± 0.33	3.27 ± 0.07	-0.80 ± 0.01	-0.80 ± 0.01	steep	
165543+194847	3.26	0.11 ± 0.01	1.97 ± 0.20	3.63 ± 0.04	-0.10 ± 0.01	-0.36 ± 0.01	flat	
165844-073917	3.74	0.83 ± 0.03	19.0 ± 1.77		+0.16 ± 0.01	-0.86 ± 0.01	peaked*	FSRQ
171521+214532	4.01	0.16 ± 0.01	6.26 ± 0.44	5.23 ± 0.03	-0.66 ± 0.01	-0.66 ± 0.01	steep	
174020+350048	3.22	0.06 ± 0.01	1.64 ± 0.29		-0.69 ± 0.01	-0.69 ± 0.01	steep	
184057+390046	3.09	0.18 ± 0.01	3.58 ± 0.33		+0.27 ± 0.01	-0.32 ± 0.01	peaked	FSRQ
193957-100241	3.78	0.59 ± 0.02	12.00 ± 1.08	3.34 ± 0.04	-0.17 ± 0.01	-0.73 ± 0.01	complex	FSRQ
200324-325144	3.77	0.68 ± 0.03	11.70 ± 1.07	3.45 ± 0.04	+0.40 ± 0.01	-0.74 ± 0.01	peaked	FSRQ
201918+112712	3.27	0.08 ± 0.01	3.14 ± 0.40		+0.71 ± 0.01	-0.84 ± 0.01	peaked	
204124+185502	3.05	0.17 ± 0.01	5.15 ± 0.62		-0.83 ± 0.01	-0.83 ± 0.01	steep	
204257-222326	3.63	0.09 ± 0.01	6.69 ± 0.86		+0.13 ± 0.01	-0.60 ± 0.02	peaked	FSRQ
204310+125513	3.27	0.14 ± 0.02	2.44 ± 0.30		-0.18 ± 0.01	-0.18 ± 0.01	flat	FSRQ
205051+312727	3.18	0.57 ± 0.03	9.89 ± 0.89		+0.15 ± 0.01	-0.39 ± 0.01	peaked	FSRQ
212912-153840	3.26	1.46 ± 0.10	6.07 ± 0.50	2.87 ± 0.04	+0.56 ± 0.01	-0.61 ± 0.01	peaked*	FSRQ
213412-041910	4.34	0.22 ± 0.01	5.15 ± 0.58	4.35 ± 0.05	-0.31 ± 0.01	-0.31 ± 0.01	flat	
221748+022010	3.57	0.32 ± 0.02	10.8 ± 1.17	4.78 ± 0.05	-0.65 ± 0.01	-0.52 ± 0.01	steep	FSRQ
221935-271903	3.63	0.21 ± 0.01	3.08 ± 0.32		-0.14 ± 0.01	-0.14 ± 0.01	flat	FSRQ
222536+204015	3.56	0.13 ± 0.01	3.79 ± 0.40	3.43 ± 0.05	-0.72 ± 0.01	-0.72 ± 0.01	steep	
224800-054118	3.29	0.20 ± 0.01	5.10 ± 0.53		+0.02 ± 0.01	-0.57 ± 0.01	peaked	bl.un.
225153+221737	3.66	0.11 ± 0.01	4.75 ± 0.47	3.96 ± 0.04	-0.36 ± 0.01	-0.36 ± 0.01	flat	FSRQ
231448+020151	4.11	0.07 ± 0.01	2.65 ± 0.40		+0.06 ± 0.01	-0.53 ± 0.01	peaked	
231643-334912	3.1	0.48 ± 0.03	1.68 ± 0.17	2.95 ± 0.04	+0.75 ± 0.02	-1.58 ± 0.01	peaked	FSRQ
232118-082721	3.16	0.18 ± 0.01	2.27 ± 0.29		-0.46 ± 0.01	-0.17 ± 0.01	flat	FSRQ
234451+343349	3.05	0.09 ± 0.01	1.62 ± 0.20		-0.50 ± 0.01	-0.50 ± 0.01	flat	

* sources with two components in the radio spectrum

Table 2. Peaked spectrum (PS) sources with their peak frequencies calculated in the observer’s frame (Col.3) and rest-frame (Col.4), flux density at the peak frequency (Col.5), PS type based solely on peak frequency value $\nu_{\text{peak,obs.}}$ (Col.6), and the reference for previous classification of an object (Col.7).

NVSS name	z	$\nu_{\text{peak,obs}}$ (GHz)	$\nu_{\text{peak,rest}}$ (GHz)	S_{peak} (Jy)	PS type	Reference
1	2	3	4	5	6	7
000657+141546	3.20	1.5	6.3	0.18	GPS	
004858+064005	3.58	3.9	17.6	0.22	GPS	Mingaliev et al. (2013)
010012−270852	3.52	1.4	6.3	0.22	GPS	
012100−280622	3.11	0.3	1.2	0.20	MPS	Mingaliev et al. (2013)
020346+113445	3.63	3.7	17.1	1.01	GPS	O’Dea et al. (1991)
021435+015703	3.28	0.5	1.9	0.25	MPS	
023220+231757	3.42	0.5	2.2	0.69	MPS	
024611+182330	3.59	1.8	8.3	0.23	GPS	
052506−334305	4.41	0.9	4.9	0.20	MPS	
053954−283955	3.10	7.0	28.7	1.08	GPS	
062419+385648	3.46	0.3	1.3	1.56	MPS	
064632+445116	3.39	17.3	76.0	3.14	GPS	O’Dea et al. (1991)
073357+045614	3.10	5.8	23.3	0.46	GPS	
075141+271632	3.20	0.2	0.8	1.85	MPS	Callingham et al. (2017)
075303+423131	3.59	0.9	4.1	1.01	MPS	Mingaliev et al. (2013)
083910+200207	3.30	1.8	7.7	0.14	GPS	
090549+041010	3.15	0.5	2.1	0.32	MPS	
093337+284532	3.42	1.7	7.5	0.11	GPS	
102623+254259	5.28	0.3	1.9	0.46	MPS	
104523+314232	3.23	0.9	3.8	0.20	MPS	
123055−113909	3.52	1.1	5.0	0.44	GPS	Mingaliev et al. (2013)
124209+372006	3.81	1.7	8.2	0.62	GPS	
130122+190353	3.10	1.7	7.0	0.13	GPS	
134022+375443	3.11	2.7	11.1	0.46	GPS	Mingaliev et al. (2013)
135406−020603	3.70	2.6	12.2	0.91	GPS	O’Dea et al. (1991)
135706−174402	3.14	1.8	7.5	1.47	GPS	O’Dea et al. (1991)
140135+151326	3.23	1.3	5.5	0.11	GPS	
140501+041535	3.20	8.3	34.9	0.82	GPS	
141821+425020	3.45	0.9	4.0	0.18	MPS	
142438+225600	3.62	3.3	15.2	0.64	GPS	O’Dea et al. (1991)
144516+095836	3.55	1.3	5.9	3.16	GPS	O’Dea et al. (1991)
150328+041949	3.66	5.6	26.1	0.17	GPS	
152117+175601	3.60	3.5	14.2	0.20	GPS	
153815+001905	3.49	2.9	13.0	0.73	GPS	Mingaliev et al. (2013)
155930+030447	3.89	4.5	22.0	0.47	GPS	Callingham et al. (2017)
160608+312504	4.56	2.5	13.9	0.92	GPS	O’Dea et al. (1991)
161637+045932	3.21	4.4	18.5	0.97	GPS	O’Dea et al. (1991)
165844−073917	3.74	5.9	28.0	0.99	GPS	O’Dea et al. (1991)
184057+390046	3.90	4.5	18.4	0.24	GPS	Marecki et al. (1999)
200324−325144	3.77	5.6	26.7	0.86	GPS	O’Dea et al. (1991)
201918+112712	3.27	0.5	2.1	0.27	MPS	
204257−222326	3.63	3.5	16.2	0.19	GPS	
205051+312727	3.18	1.9	7.9	0.83	GPS	
212912−153840	3.26	6.8	28.9	1.44	GPS	O’Dea et al. (1991)
224800−054118	3.29	0.4	1.7	0.91	MPS	Callingham et al. (2017)
231448+020151	4.11	1.7	8.7	0.12	GPS	
231643−334912	3.10	3.9	16.0	0.73	GPS	Mingaliev et al. (2013)

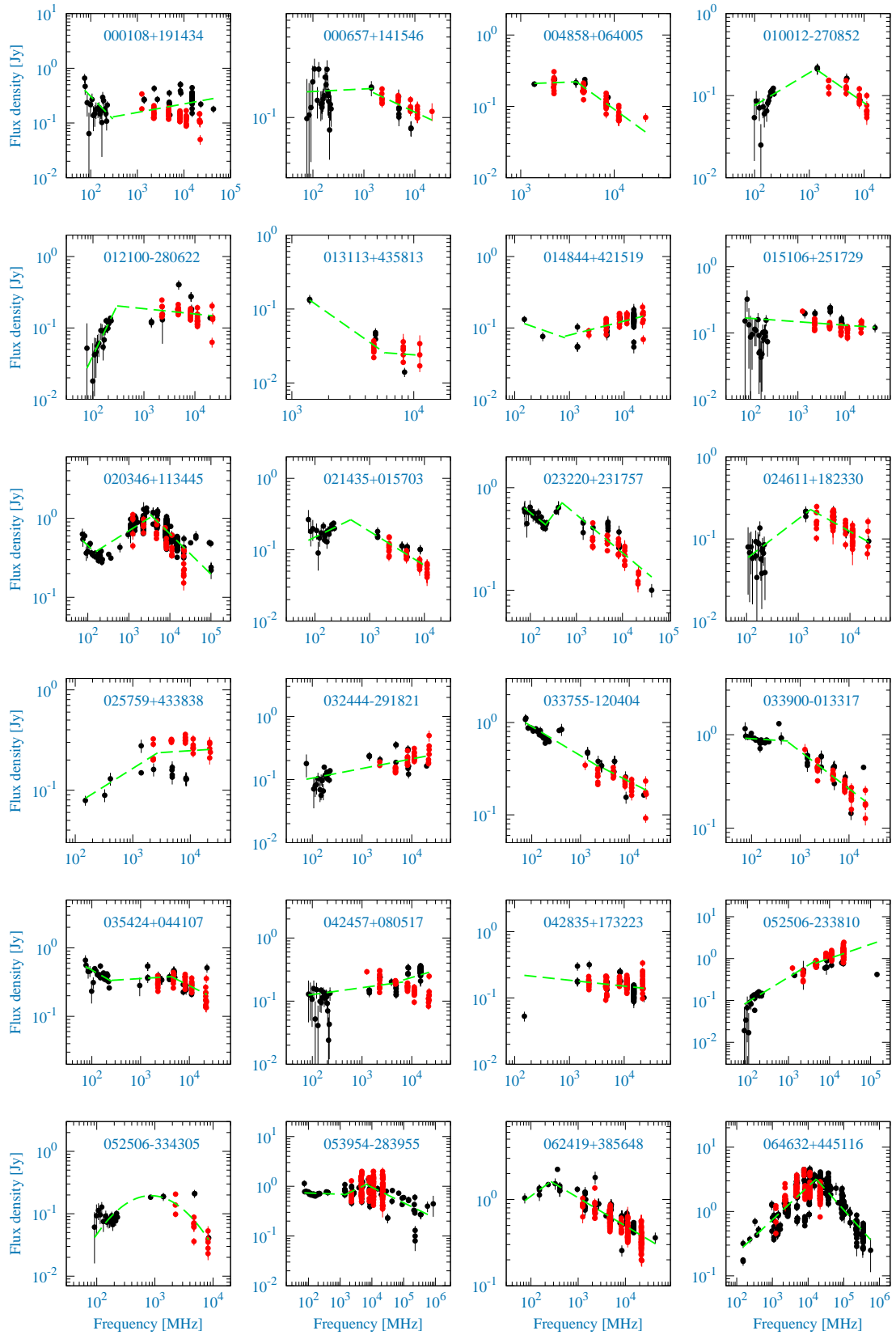
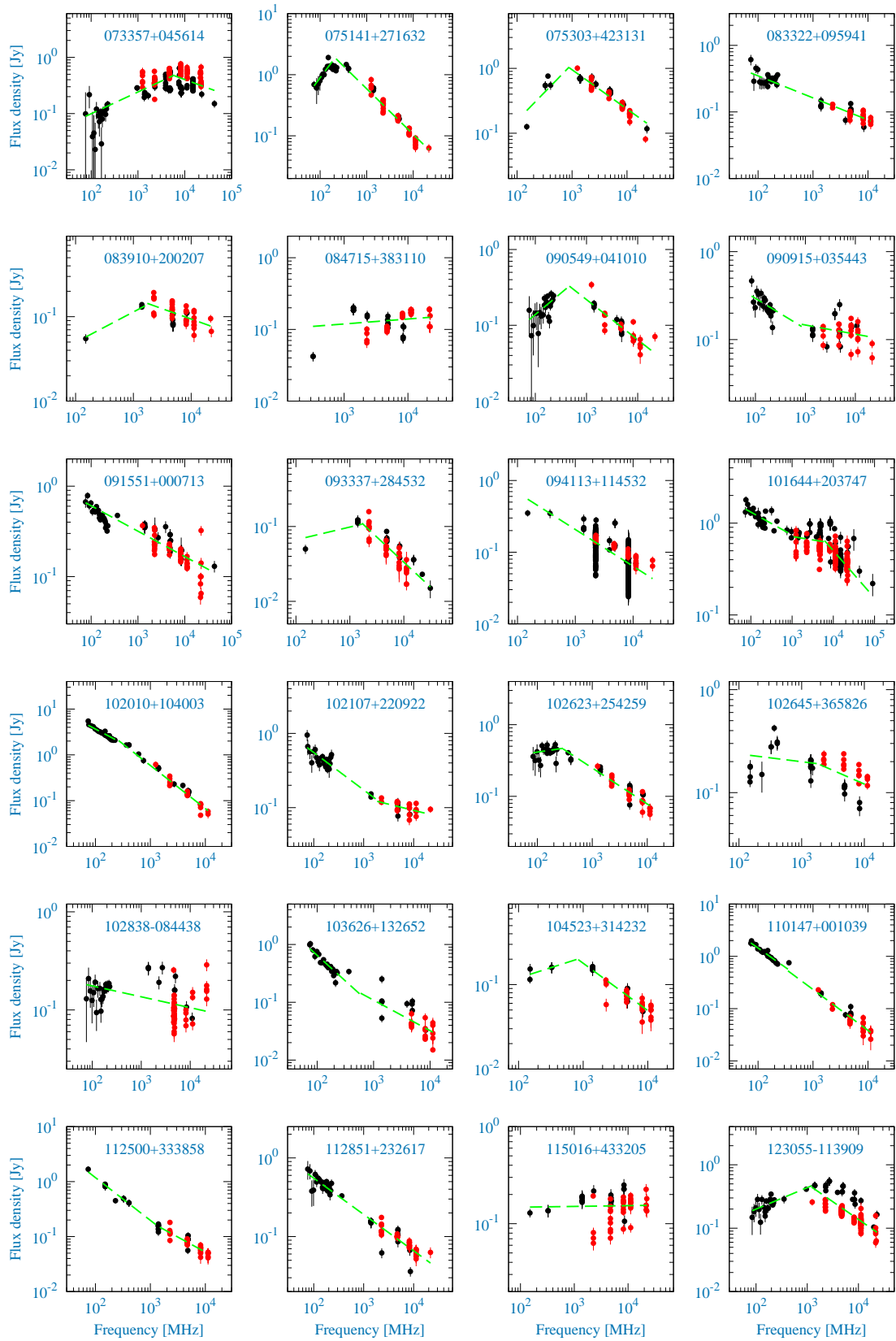


Figure 1. Broad-band radio spectra of the quasars. RATAN-600 data are shown with red circles and literature data are shown with black circles. The green dashed line represents a linear or parabolic fit to the radio spectrum.



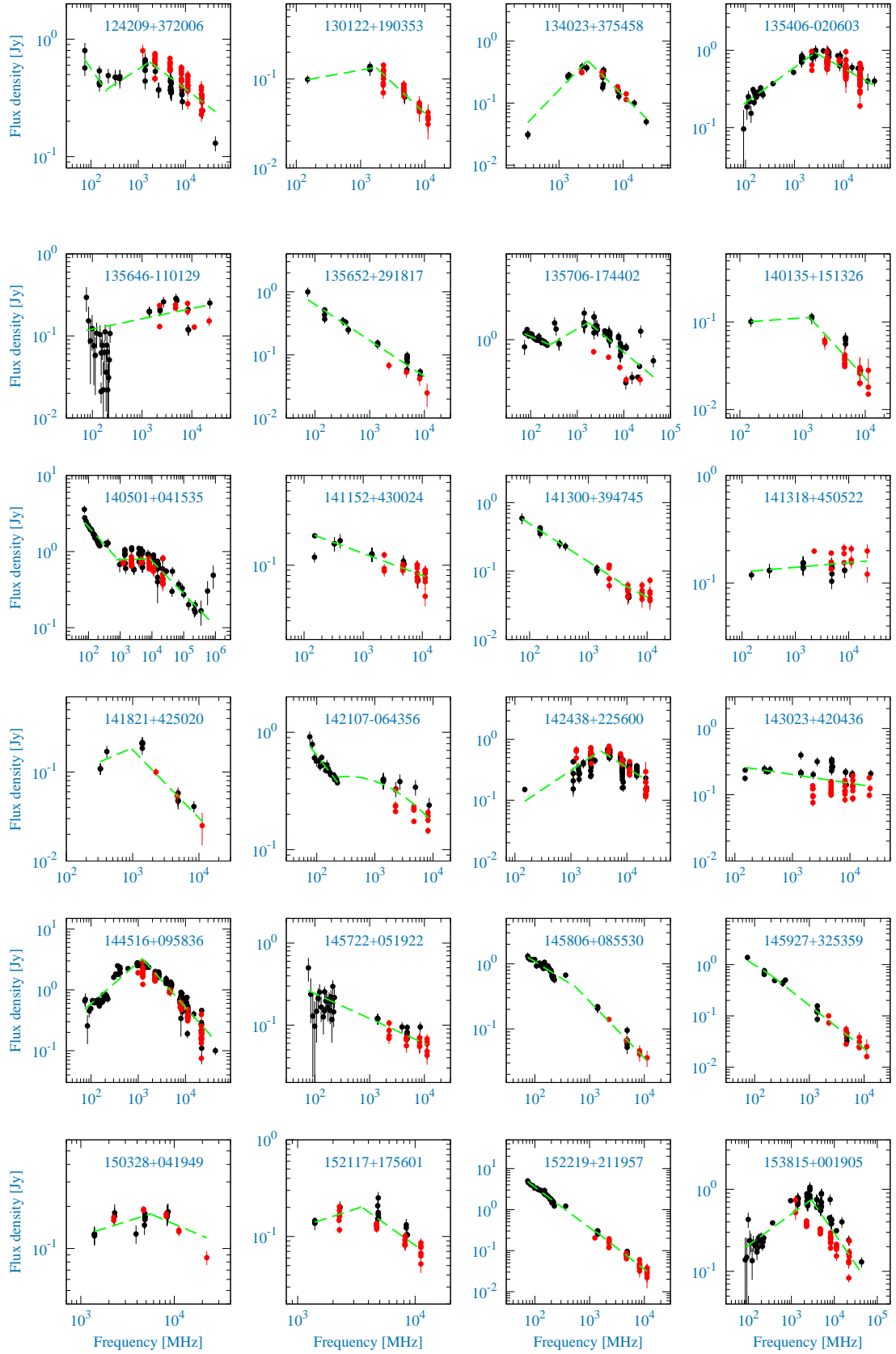
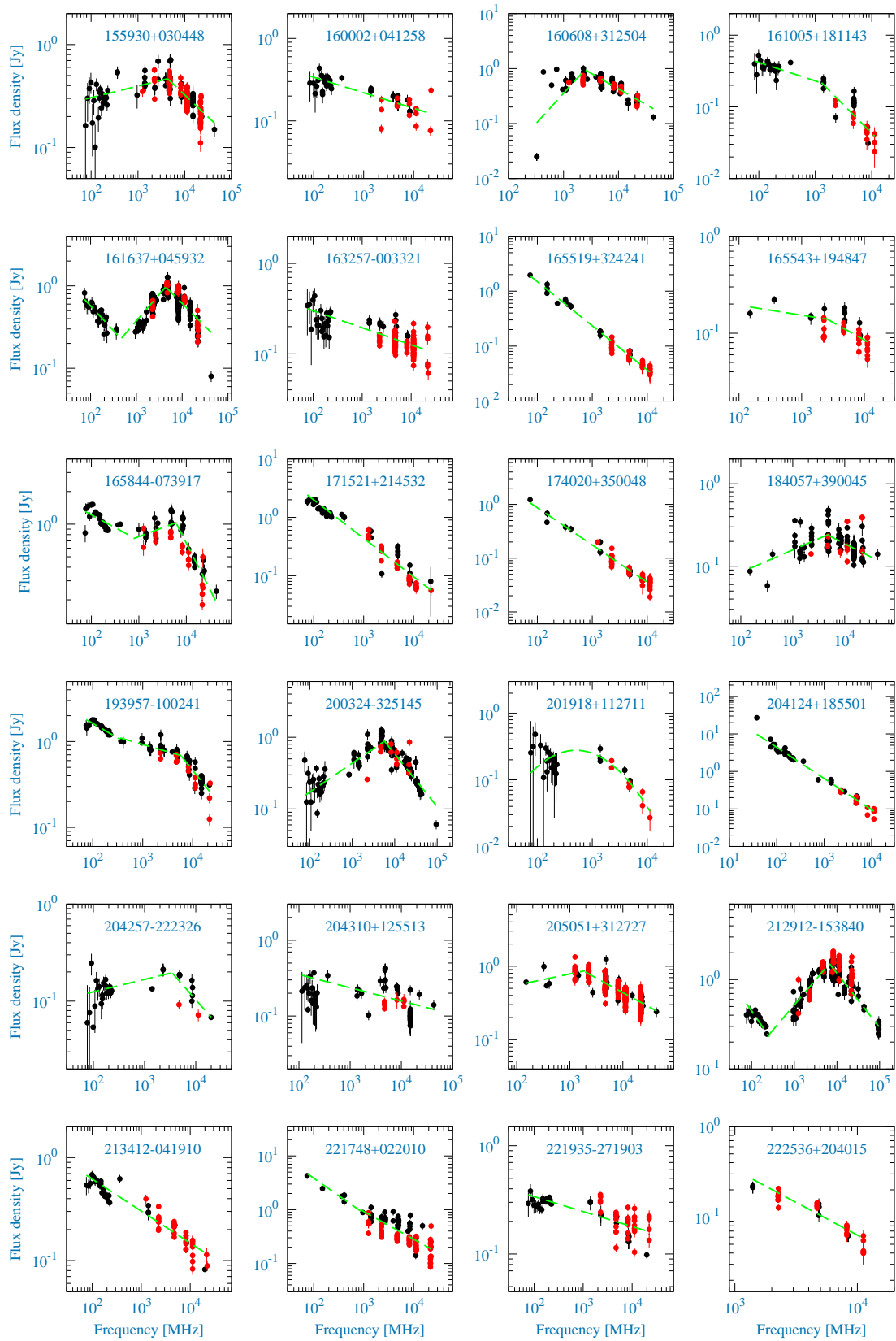


Figure 3. Broad-band radio spectra of the quasars. The description for symbols and lines is the same as in Fig. 1.



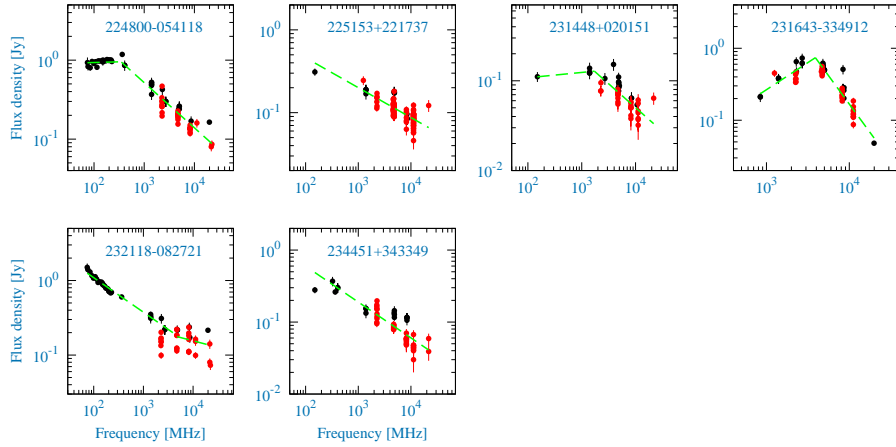


Figure 5. Broad-band radio spectra of the quasars. The description for symbols and lines is the same as in Fig. 1.

This paper has been typeset from a $\text{\TeX}/\text{\LaTeX}$ file prepared by the author.